

Isovalent substitution modulates average and short-range structure in disordered rocksalt oxides

John D. Langhout,[†] Elizabeth Gager,[†] Talianna Ulloa,[‡] Shane Shepard,[†]
Juan C. Nino,[†] and Megan M. Butala^{*,†}

[†]*Department of Materials Science and Engineering, University of Florida, Gainesville, FL
32611*

[‡]*Department of Electrical and Computer Engineering, University of Florida, Gainesville, FL
32611*

E-mail: mbutala@ufl.edu

Supplementary Information

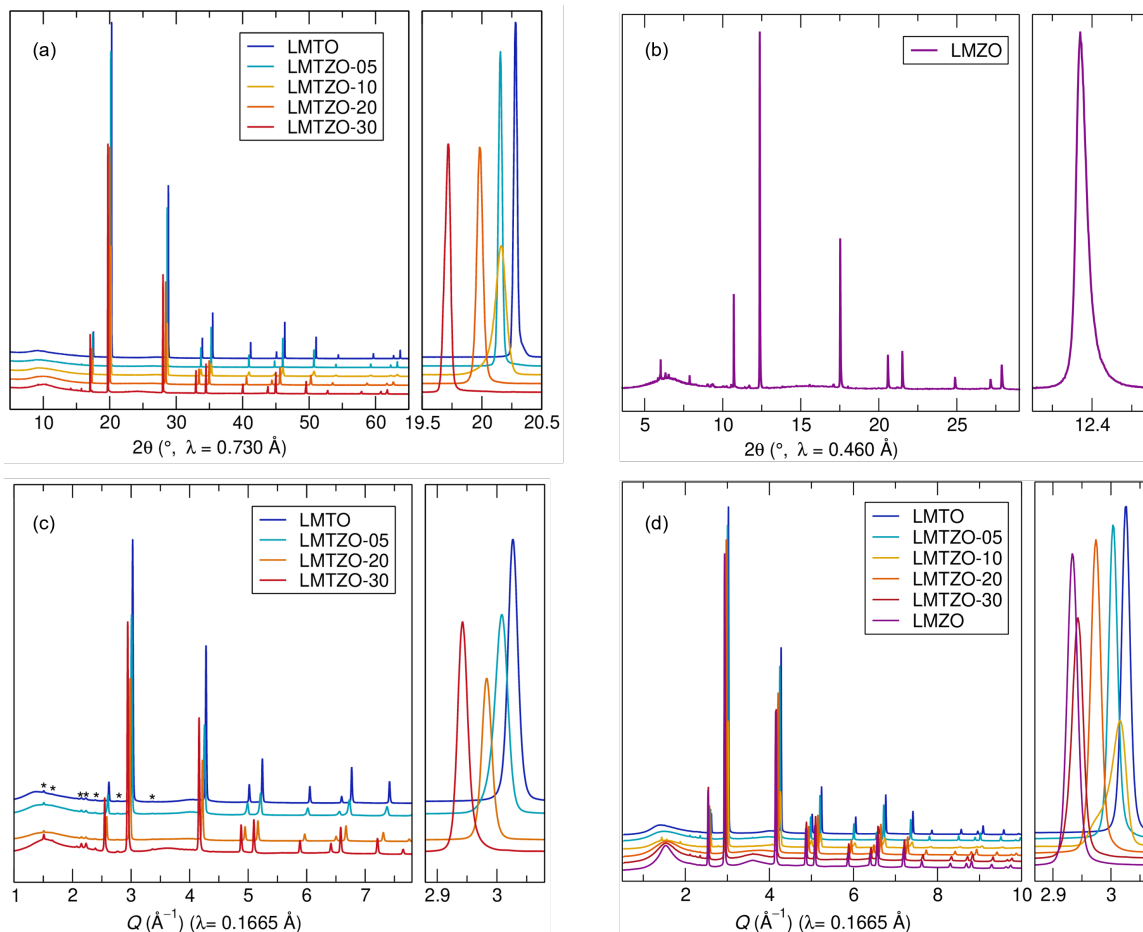
LMTZO sample sets

During the course of this study, syntheses of all compositions were repeated to complete the range of structural, chemical, and electrochemical experiments. Due to slightly different synthesis conditions (i.e., slower furnace cooling rate in a larger tube furnace) and material storage conditions (powders should be stored in an air-free environment such as an Ar glovebox), diffraction peak shapes and impurities varied slightly between powder sample sets. X-ray diffraction (XRD) data of each sample set are shown in Fig. S1.

Qualitatively, diffraction data differ between sets, particularly in peak broadness and, related, their relative intensities. This can be partly attributed to the data being collected at different beamlines with different instrument broadening, but there are structural origins as well. Nonetheless, we regard samples from the two sets as interchangeable, except for LMZO, for which only data from the second sample set is considered. Results from Rietveld refinement and PDF small-box modeling for each composition were consistent between datasets, with only minor differences in the main phase structure and minimal impurity phases present; the fundamental takeaways and trends across the compositional series are unchanged by these minor differences. Regardless, we will present here which presented data are taken from which sample set:

In the manuscript, Fig. 1 contains data collected at beamline #2-1 at SSRL for all samples except for LMZO, for which data was collected at beamline 28-ID-1 at NSLS-II. These are also the XRD data on which reported Rietveld refinements were performed.

All scanning electron microscopy (SEM) data are from the first sample set after an extended period of storage in air, hence the Li_2CO_3 impurities. All PDF data shown and refined are of the second sample set using data collected at beamline 28-ID-1 at NSLS-II. Preliminary PDF data of the first sample set, taken during a mail-in experiment at 11-ID-B, were also analyzed, but omitted from this manuscript due to the dataset being incomplete.



All batteries used powders from the second sample set.

Rietveld refinements

Rietveld refinements for LMTZO-05 and LMTZO-10 are in the main body of the paper. Refinements of the other compositions, and the beamlines the data are from, are provided here for reference.

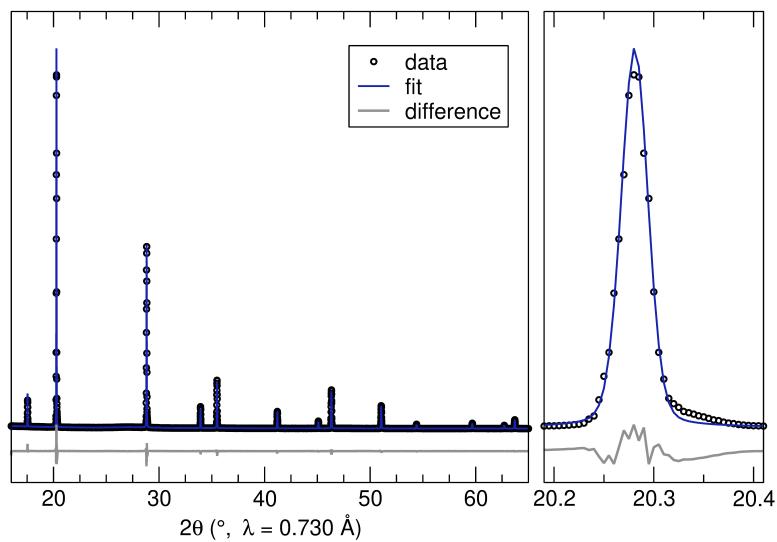


Figure S2: Rietveld refinement of synchrotron XRD data (SSRL, beamline #2-1) for LMTO fit to a DRX model. Refined parameters are in Table S1

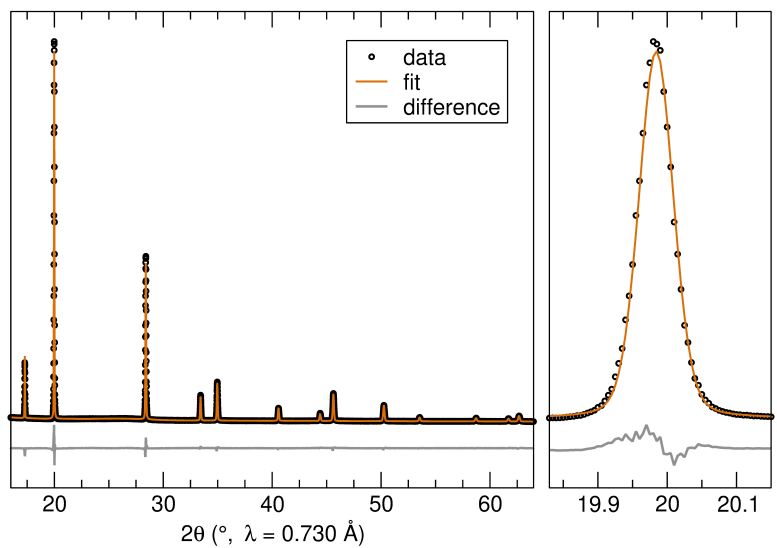


Figure S3: Rietveld refinement of synchrotron XRD data (SSRL, beamline #2-1) for LMTZO-20 fit to a DRX model. Refined parameters are in Table S4

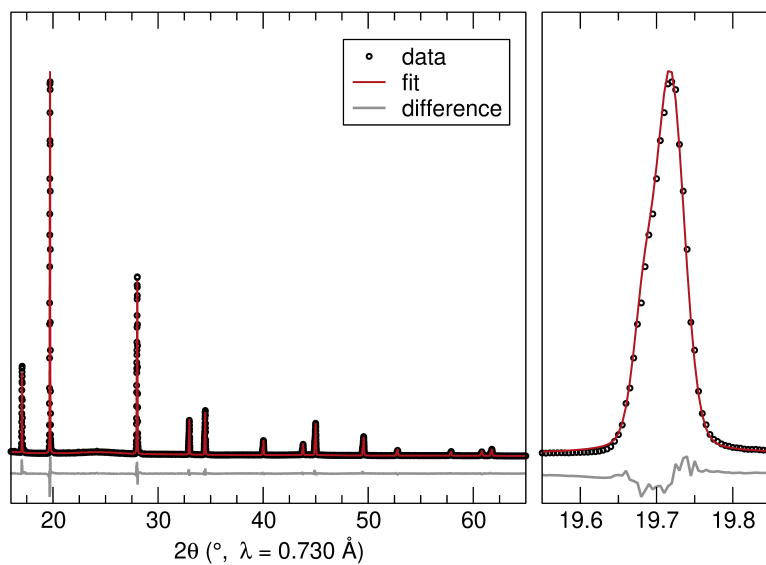


Figure S4: Rietveld refinement of synchrotron XRD data (SSRL, beamline #2-1) for LMTZO-30 fit to a two-phase DRX model. Refined parameters are in Table S5

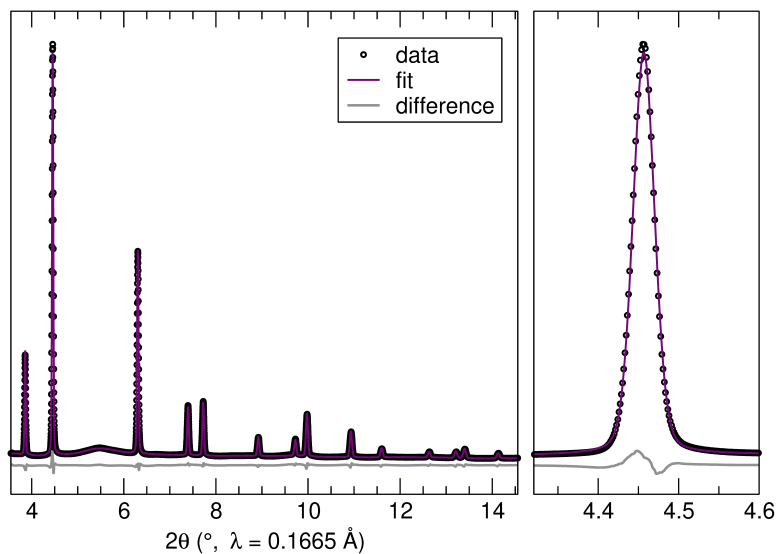


Figure S5: Rietveld refinement of synchrotron XRD data (NSLS-II, beamline 28-ID) for LMZO fit to a DRX model. Refined parameters are in Table S6

Rietveld refinement fitting parameters

For Rietveld refinement of XRD data, the lattice parameter (a), isotropic atomic displacement parameters (U_{iso}), and microstrain ($\mu strain$) were refined for all compositions. U_{iso} of all cations were constrained to be equal, since they share a single crystallographic site. LG_{mix} , which models peak shape (*i.e.*, strain distribution) as a mix between Gaussian and Lorentzian functions, was constrained to be 0 for the main phases of LMTO, LMTZO-05, LMTZO-10, and LMTZO-30, but was refined between 0 and 1 to better capture peak shapes of LMTZO-20 and LMZO and the secondary phases of LMTZO-10 and LMTZO-30. Refined parameters are shown in Tables S1, S2, S3, S4, S5, and S6.

Table S1: Data and refinement information for LMTO.

LMTO, $Fm\bar{3}m$					
$w_R = 6.077\%$, beamline #2-1, SSRL					
$a = 4.149591(13) \text{ \AA}$					
$\mu strain = 867.4$, $LG_{mix} = 0$					
Atom	x	y	z	occ	U_{iso}
Li	0	0	0	0.6	0.00857(5)
O	0.5	0.5	0.5	1	0.01434(11)
Ti	0	0	0	0.2	0.00857(5)
Mn	0	0	0	0.2	0.00857(5)

Table S2: Data and refinement information for LMTZO-05.

LMTZO-05, $Fm\bar{3}m$					
$w_R = 4.312\%$, beamline #2-1, SSRL					
$a = 4.175177(9) \text{ \AA}$					
$\mu strain = 1390.9$, $LG_{mix} = 0$					
Atom	x	y	z	occ	U_{iso}
Li	0	0	0	0.6	0.01027(4)
O	0.5	0.5	0.5	1	0.01780(9)
Ti	0	0	0	0.175	0.01027(4)
Mn	0	0	0	0.2	0.01027(4)
Zr	0	0	0	0.025	0.01027(4)

Table S3: Data and refinement information for LMTZO-10.

LMTZO-10					
$w_R = 4.46\%$, beamline #2-1, SSRL					
Primary Phase ($Fm\bar{3}m$)					
$a = 4.169360(19) \text{ \AA}$					
$\mu_{strain} = 7666.1, LG_{mix} = 0$					
Wt. fraction = 0.7476(23)					
Atom	x	y	z	occ	U_{iso}
Li	0	0	0	0.6	0.01710(11)
O	0.5	0.5	0.5	1	0.01985(19)
Ti	0	0	0	0.15	0.01710(11)
Mn	0	0	0	0.2	0.01710(11)
Zr	0	0	0	0.05	0.01710(11)
Secondary Phase ($Fm\bar{3}m$)					
$a = 4.18208(15) \text{ \AA}$					
$\mu_{strain} = 15564.4, LG_{mix} = 0.151$					
Wt. fraction = 0.2524(23)					
Atom	x	y	z	occ	U_{iso}
Li	0	0	0	0.6	0.00016(11)
O	0.5	0.5	0.5	1	0.0100(3)
Ti	0	0	0	0.15	0.00016(11)
Mn	0	0	0	0.2	0.00016(11)
Zr	0	0	0	0.05	0.00016(11)

Table S4: Data and refinement information for LMTZO-20.

LMTZO-20, $Fm\bar{3}m$					
$w_R = 4.033\%$, beamline #2-1, SSRL					
$a = 4.210813(6) \text{ \AA}$					
$\mu_{strain} = 5141.0, LG_{mix} = 0.164$					
Atom	x	y	z	occ	U_{iso}
Li	0	0	0	0.6	0.01105(4)
O	0.5	0.5	0.5	1	0.01808(10)
Ti	0	0	0	0.175	0.01105(4)
Mn	0	0	0	0.2	0.01105(4)
Zr	0	0	0	0.025	0.01105(4)

Table S5: Data and refinement information for LMTZO-30.

LMTZO-30					
$w_R = 4.869\%$, beamline #2-1, SSRL					
Primary Phase ($Fm\bar{3}m$)					
$a = 4.265979(17) \text{ \AA}$					
$\mu_{strain} = 2641.4$, $LG_{mix} = 0$					
Phase fraction = 0.8324(20)					
Atom	x	y	z	occ	U_{iso}
Li	0	0	0	0.6	0.01181(6)
O	0.5	0.5	0.5	1	0.02343(17)
Ti	0	0	0	0.05	0.01181(6)
Mn	0	0	0	0.2	0.01181(6)
Zr	0	0	0	0.15	0.01181(6)
Secondary Phase ($Fm\bar{3}m$)					
$a = 4.273567(23) \text{ \AA}$					
$\mu_{strain} = 395.8$, $LG_{mix} = 0.5$					
Phase fraction = 0.1676(20)					
Atom	x	y	z	occ	U_{iso}
Li	0	0	0	0.6	0.00659(15)
O	0.5	0.5	0.5	1	0.0326(5)
Ti	0	0	0	0.05	0.00659(15)
Mn	0	0	0	0.2	0.00659(15)
Zr	0	0	0	0.15	0.00659(15)

Table S6: Data and refinement information for LMZO.

LMZO, $Fm\bar{3}m$					
$w_R = 3.165\%$, beamline 28-ID-1, NSLS-II					
$a = 4.28008(4) \text{ \AA}$					
$\mu_{strain} = 9302.7$, $LG_{mix} = 0.216$					
Atom	x	y	z	occ	U_{iso}
Li	0	0	0	0.6	0.01116(5)
O	0.5	0.5	0.5	1	0.02031(13)
Mn	0	0	0	0.2	0.01116(5)
Zr	0	0	0	0.2	0.01116(5)

SEM/particle analysis

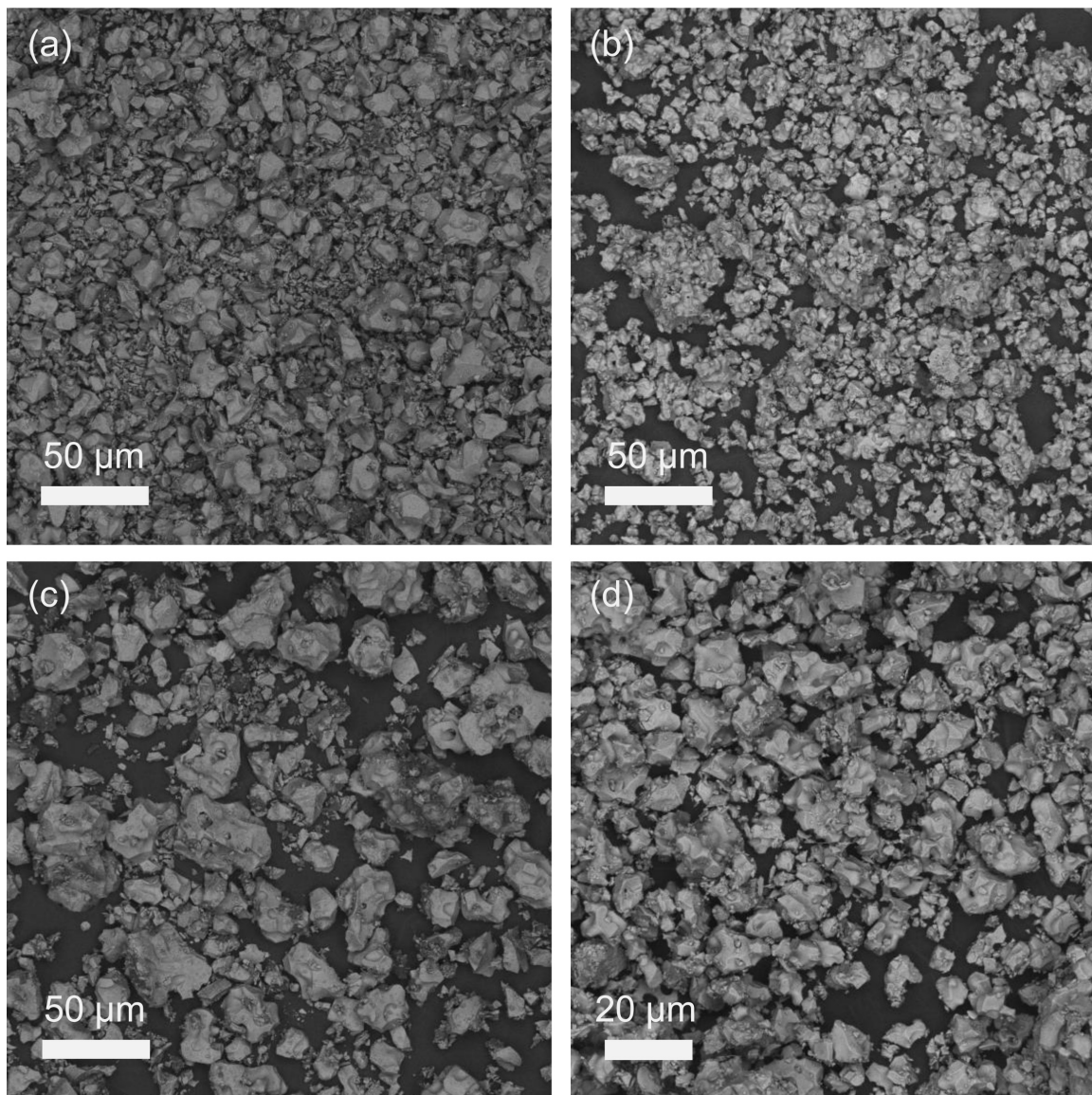


Figure S6: Additional BSE SEM micrographs of (a) LMTO, (b) LMTZO-05, (c) LMTZO-10, and (d) LMTZO-20.

In BSE micrographs of LMTZO-30, three distinct particles or domains were detected (Fig. S7). EDS spot analysis demonstrated that most of the phase was the expected LMTZO-30 rocksalt, with expected concentrations of transition metals. Spot analysis of darker regions yielded signal only for O and C. Samples were carbon coated, so impurity could be either Li_2O or Li_2CO_3 , but since only Li_2CO_3 impurities were detected in XRD

data, we conclude that this impurity is Li_2CO_3 . Infrequent bright particles of unique morphology were also detected. Spot analysis revealed this to be a silver paste contaminant, most likely from contact with other SEM samples and equipment.

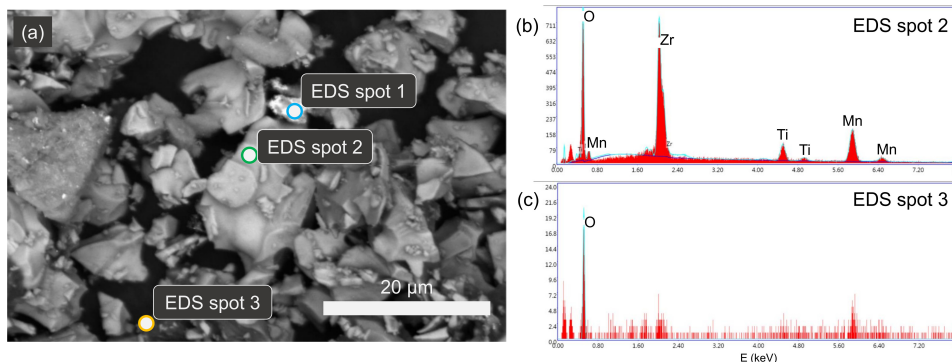


Figure S7: BSE SEM micrograph of LMTZO-30 with spot EDS of main phase and darker impurity phase. (a) Main phase (“EDS Spot 2”) shows expected concentrations of transition metals. (b) Impurity phase (“EDS Spot 3”) only shows O and C. “EDS Spot 1” was a silver paste contaminant.

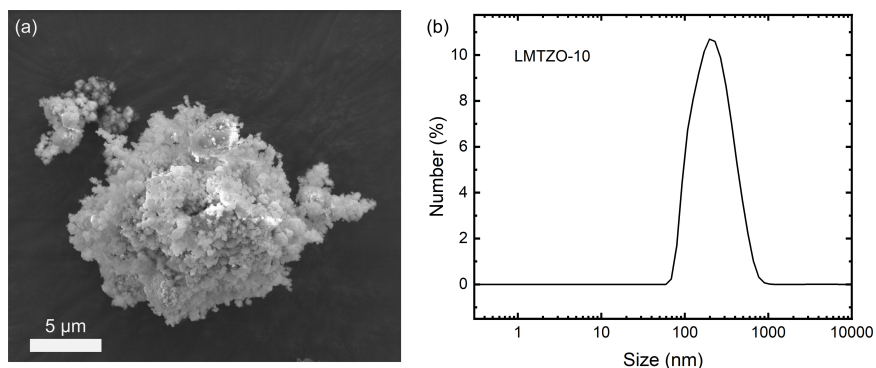


Figure S8: (a) SE SEM micrograph of ball-milled powders (LMTZO-10 + C) show successful particle downsizing. (b) Accompanying dynamic light scattering also shows range of cathode particle size after ball milling (100 nm to 1000 nm) as well as presence of secondary particles composed of agglomerated nano-sized particles.

Pair distribution function analysis

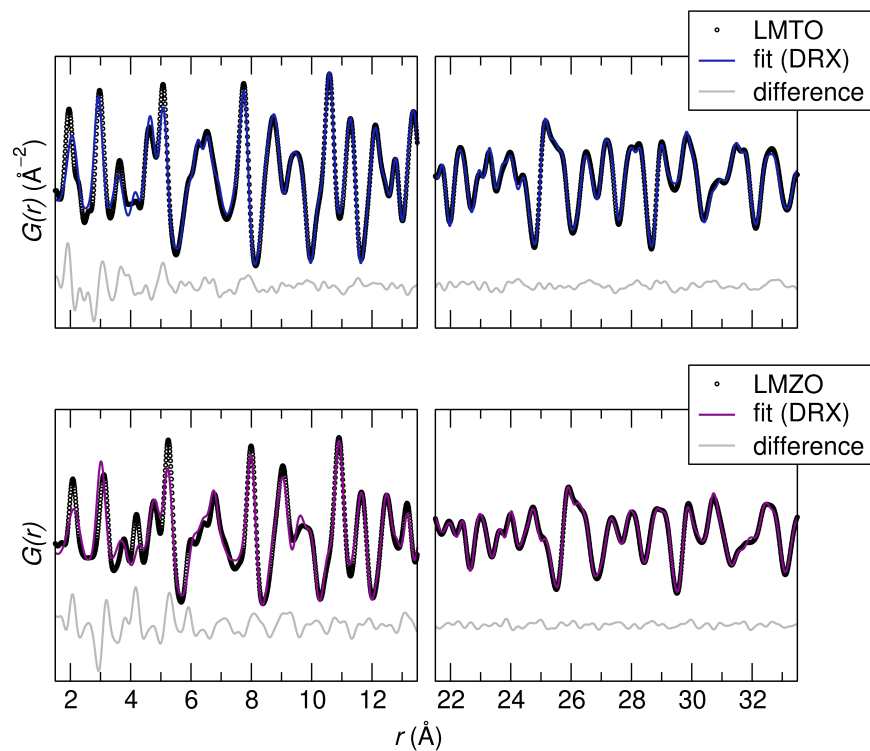


Figure S9: PDF data of LMTO (top) and LMZO (bottom) and fits to a cation-disordered cubic rocksalt model over the entire PDF (1.7 \AA to 60 \AA). Short- and medium- (1.5 \AA to 13.5 \AA) and long-range (21.5 \AA to 33.5 \AA) sections show r -dependence of fit quality.

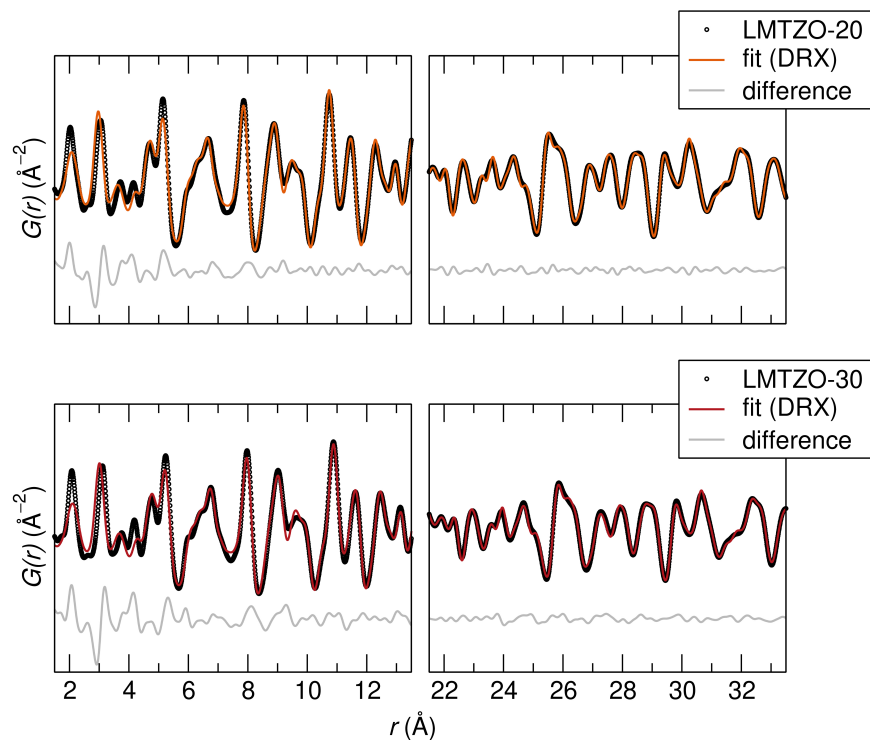


Figure S10: PDF data of LMTZO-20 (top) and LMTZO-30 (bottom) and fits to a cation-disordered cubic rocksalt model over the entire PDF (1.7 Å to 60 Å). Short- and medium- (1.5 Å to 13.5 Å) and long-range (21.5 Å to 33.5 Å) sections show r -dependence of fit quality.

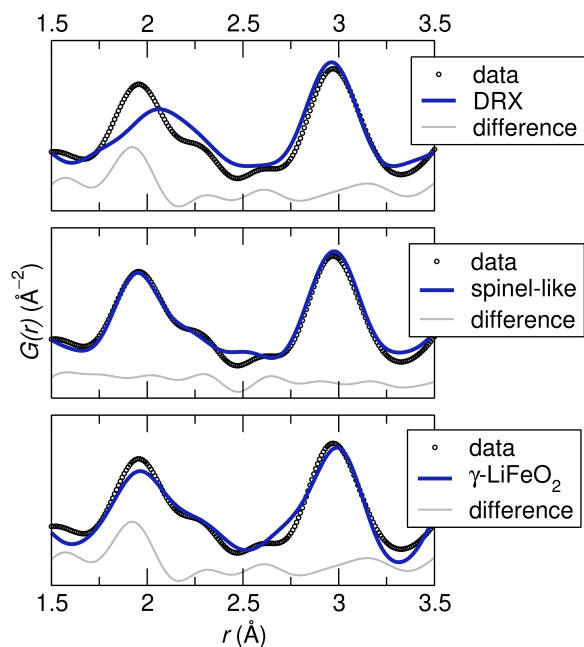


Figure S11: Local-range fits of DRX, Li_2MnO_3 , and $\gamma\text{-LiFeO}_2$ models to the PDF of LMTO.

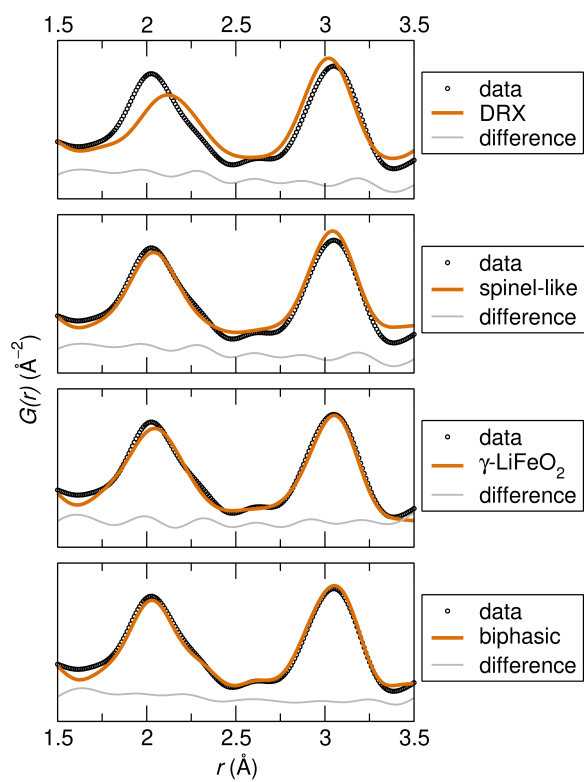


Figure S12: Local-range fits of DRX, Li_2MnO_3 , γ -LiFeO₂, and biphasic models to the PDF of LMTZO-20.

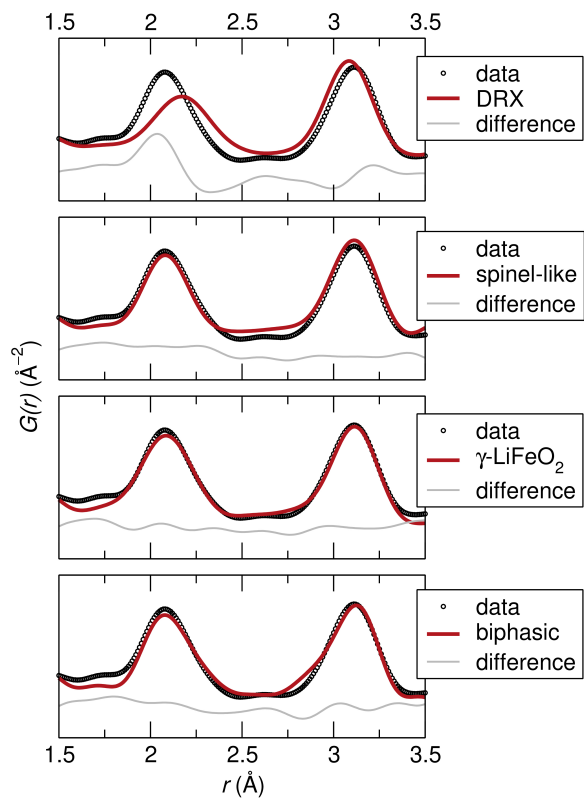


Figure S13: Local-range fits of DRX, Li_2MnO_3 , $\gamma\text{-LiFeO}_2$, and biphasic models to the PDF of LMTZO-30.

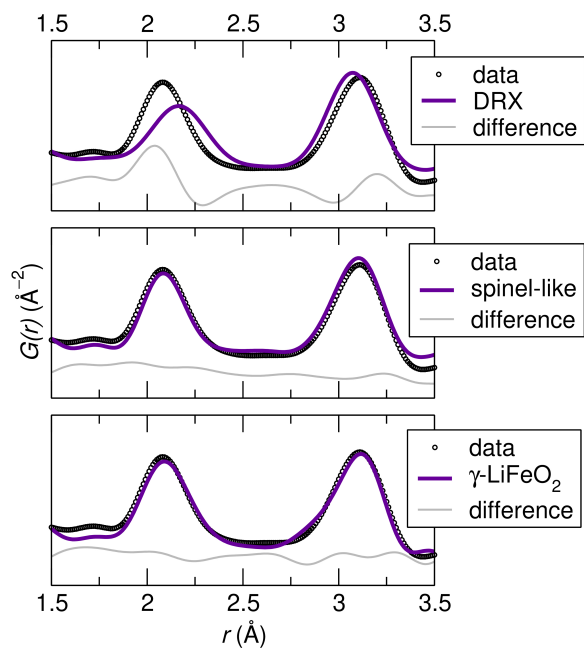


Figure S14: Local-range fits of DRX, Li_2MnO_3 , and $\gamma\text{-LiFeO}_2$ models to the PDF of LMZO.

Following are the SRO models (Li_2MnO_3 and $\gamma\text{-LiFeO}_2$) which were fit to the local range PDFs of LMTO and LMZO, respectively. Lattice parameter (a , c), O-site position, U_{iso} of Ti/Mn, Zr, and O were refined in these structures.

Table S7: Refined fitting parameters of the ‘ Li_2MnO_3 ’ structure fit to local-range LMTO (Fig. S11).

“ Li_2MnO_3 ,” $I4_1/amd$				
LMTO				
$a = b = 5.857370 \text{ \AA}$				
$c = 9.280540 \text{ \AA}$				
$\alpha = \beta = \gamma = 90^\circ$				
Atom	x	y	z	occ
Li	0	0.750000	0.625000	1.0
Li	0	0.250000	0.125000	0.2
O	0	0.781822	0.888094	1.0
Ti	0	0.250000	0.125000	0.4
Mn	0	0.250000	0.125000	0.4

Table S8: Refined fitting parameters of the ‘ $\gamma\text{-LiFeO}_2$ ’ structure fit to local-range LMZO (Fig. S14).

“ $\gamma\text{-LiFeO}_2$,” $I4_1/amd$				
LMZO				
$a = b = 3.957020 \text{ \AA}$				
$c = 9.466550 \text{ \AA}$				
$\alpha = \beta = \gamma = 90^\circ$				
Atom	x	y	z	occ
Li	0	0	0	1.0
Li	0	0	0.500000	0.2
O	0	0	0.258897	1.0
Mn	0	0	0.500000	0.4
Zr	0	0	0.500000	0.4

The distance of the second atomic correlation in the PDFs is known to be related to chemical SRO.¹ More ordered DRXs will favor *TM*-Li next-nearest neighbors. In comparison, more disordered DRXs have a higher proportion of *TM-TM* next-nearest neighbors; these high-valence cations tend to repel one another, increasing the second-nearest neighbor correlation distance. The next-nearest neighbor correlation distances from PDF and XRD data are in Table S9. From PDF data, the center of the second correlation was measured; from XRD data, distances were calculated using the refined unit cell lattice parameter, a .

Table S9: Next-nearest neighbor atomic correlation distances from PDF and XRD data and their differences.

composition	distance from PDF (Å)	distance from XRD (Å)	difference (Å)
LMTO	2.97	2.93	0.04
LMTZO-05	3.00	2.95	0.05
LMTZO-10	3.00	2.95	0.05
LMTZO-20	3.05	2.98	0.07
LMTZO-30	3.11	3.02	0.09
LMZO	3.11	3.03	0.08

Battery Cycling

Batteries were cycled at a $C/10$ rate for 50 cycles. Representative voltage curves showing all 50 cycles for each composition are shown in Fig. S15, S16, S17, S18, S19, and S20.

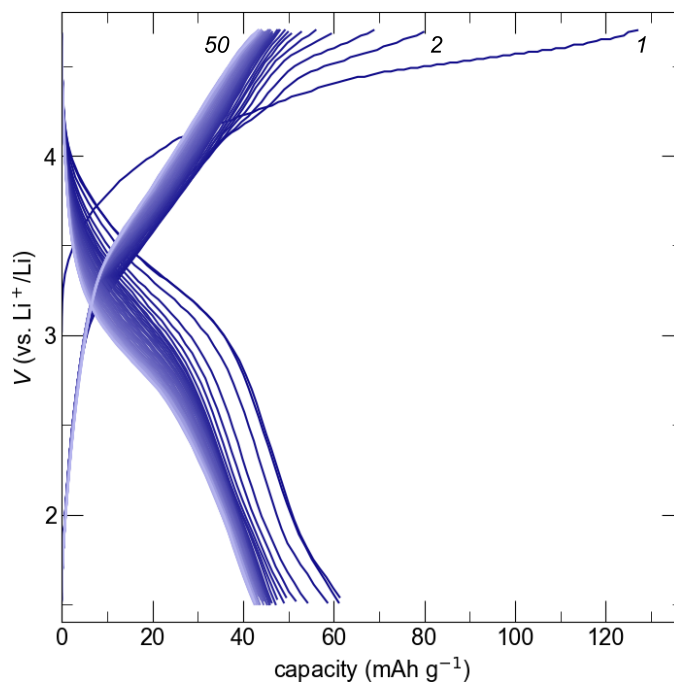


Figure S15: Voltage profiles of $C/10$ cycling for LMTO for the first 50 cycles.

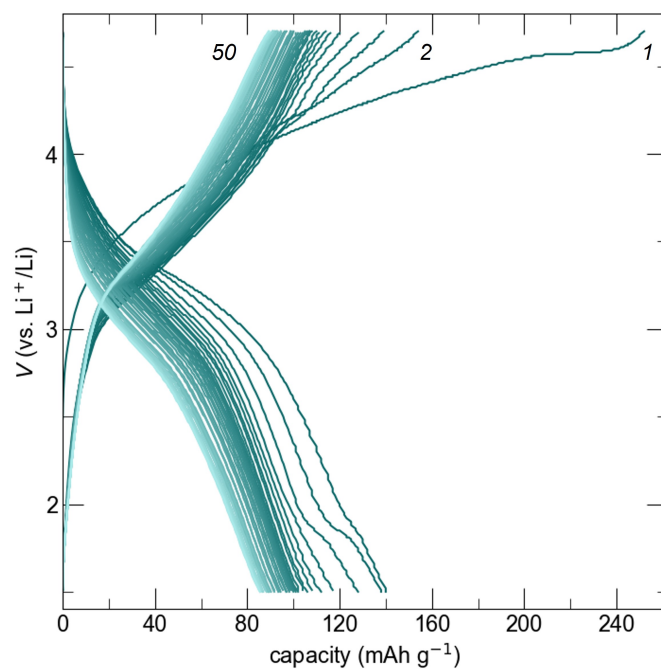


Figure S16: Voltage profiles of $C/10$ cycling for LMTZO-05 for the first 50 cycles.

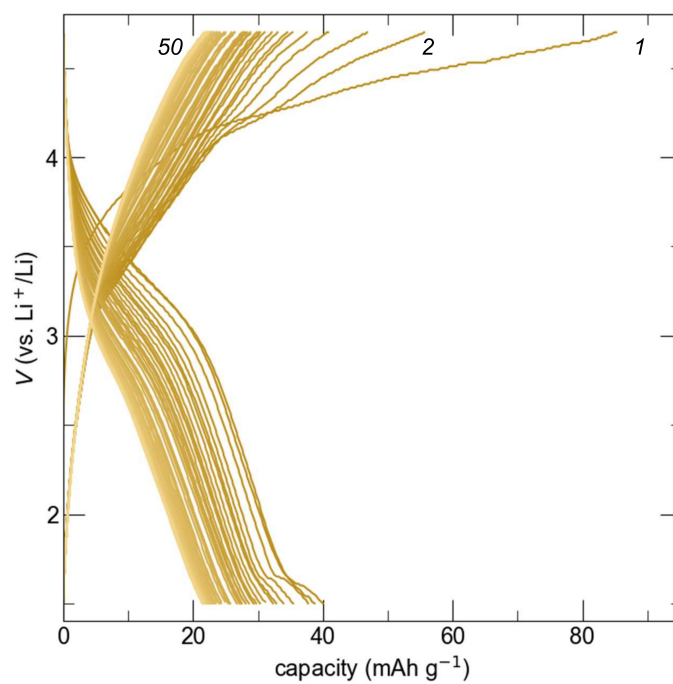


Figure S17: Voltage profiles of $C/10$ cycling for LMTZO-10 for the first 50 cycles.

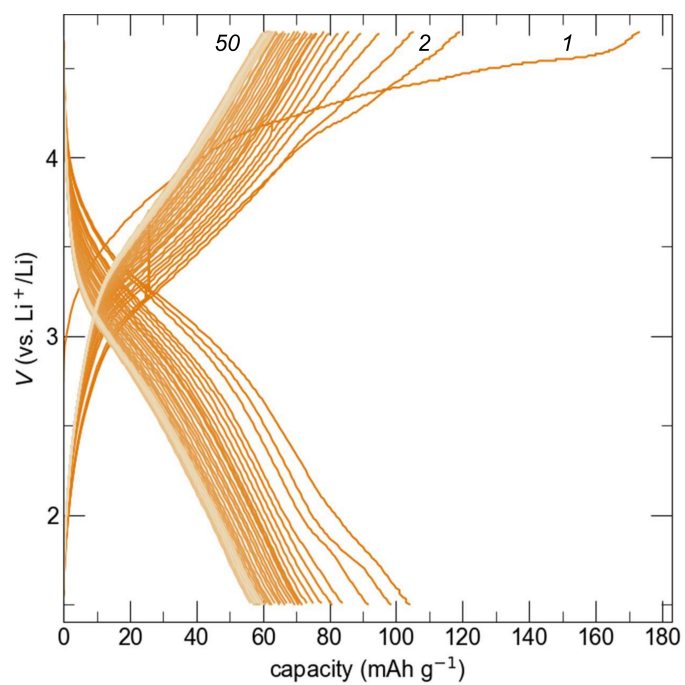


Figure S18: Voltage profiles of $C/10$ cycling for LMTZO-20 for the first 50 cycles.

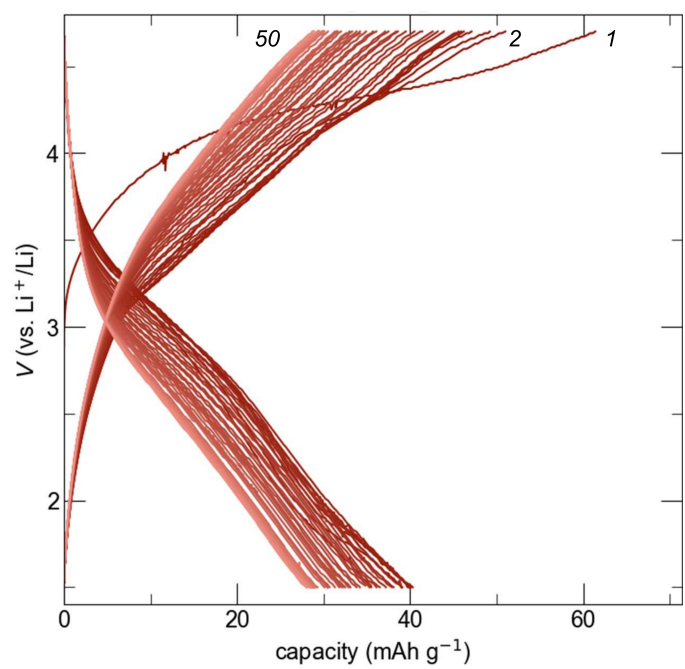


Figure S19: Voltage profiles of $C/10$ cycling for LMTZO-30 for the first 50 cycles.

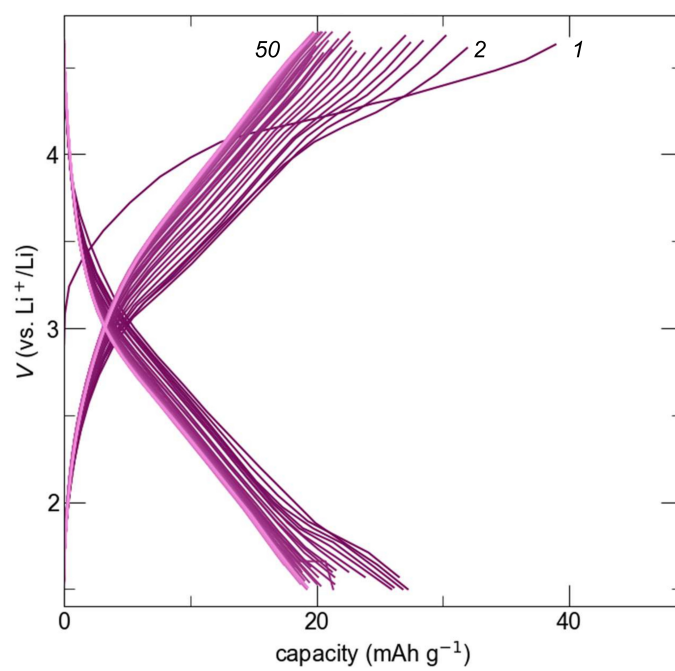


Figure S20: Voltage profiles of $C/10$ cycling for LMZO for the first 50 cycles.

Ex situ XRD

To investigate whether the plateaus at low voltage observed in some discharge profiles corresponded to a phase transformation, *ex situ* lab XRD was performed on cycled cathode pellets (Fig. S21). No visible phase transformation was apparent in these data.

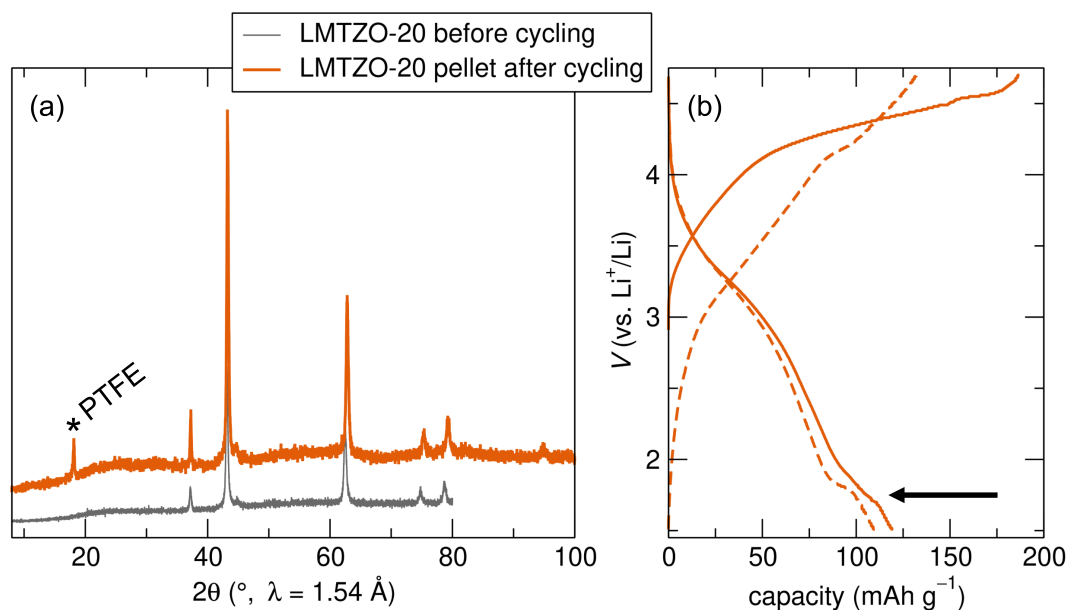


Figure S21: (a) Lab source XRD of ball milled cathode powder (LMTZO-20 and SuperC65) and *ex situ* cycled cathode. The only notable difference between the patterns is the emergence of a peak at $2\theta = 18^\circ$, which corresponds to the PTFE binder.² (b) First two cycles of the same cathode (C/10), with an arrow denoting the low-voltage plateau of interest.

Electrochemical Impedance Spectroscopy

Electrochemical impedance spectroscopy (EIS) was performed on cells prior to cycling. While cell impedances (and accompanying equivalent circuits) varied significantly across cells, there was no clear dependency between qualitative Nyquist plot size/shape and cell capacity. Shown are the Nyquist plots for three LMTZO-30 cells (Fig. S22). While the data show variability of cell impedance, this does not translate to an equivalent variability in first discharge capacity.

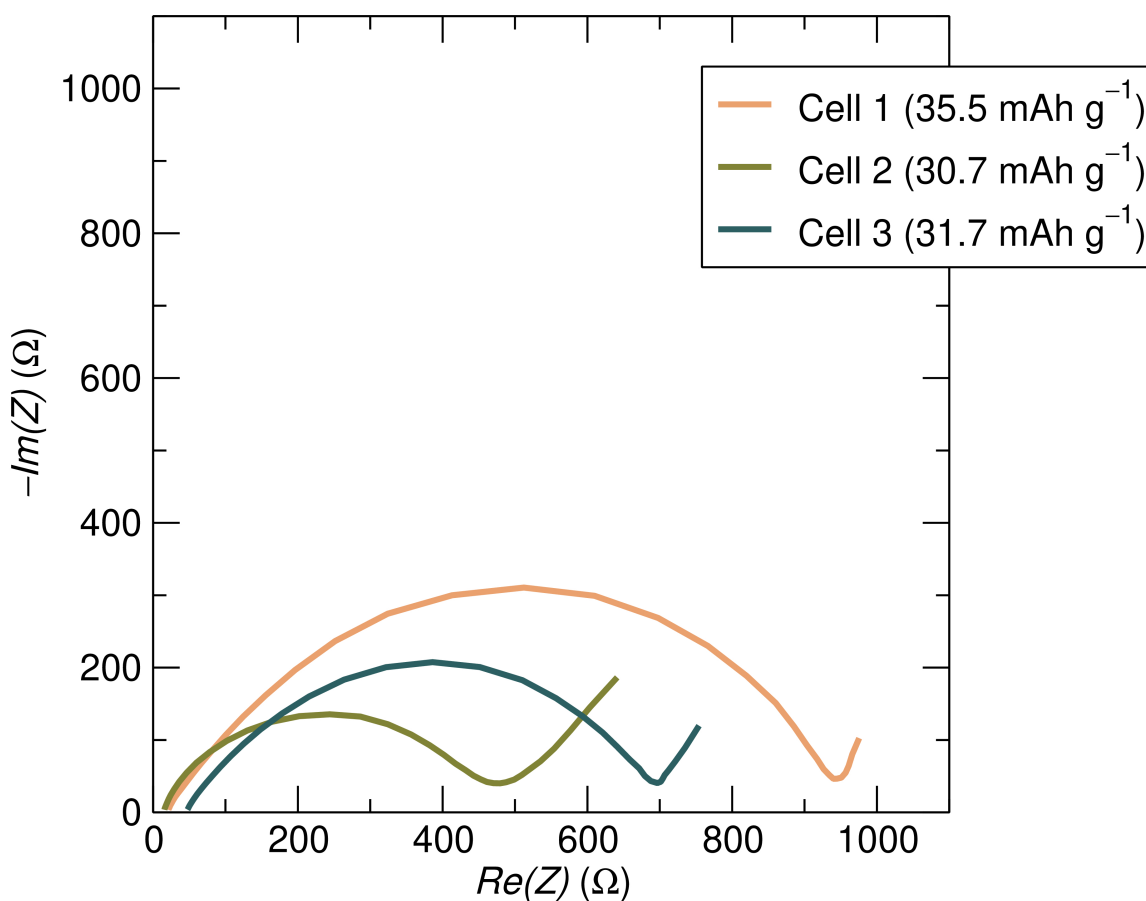


Figure S22: Nyquist plots of EIS measurements on three LMTZO-30 cells. Each dataset labeled with corresponding first discharge capacity.

References

- (1) Szymanski, N. J.; Lun, Z.; Liu, J.; Self, E. C.; Bartel, C. J.; Nanda, J.; Ouyang, B.; Ceder, G. Modeling Short-Range Order in Disordered Rocksalt Cathodes by Pair Distribution Function Analysis. *Chem. Mater.* **2023**, *35*, 4922–4934.
- (2) Wang, R.; Huang, B.; Qu, Z.; Gong, Y.; He, B.; Wang, H. Research on the kinetic properties of the cation disordered rock-salt Li-excess $\text{Li}_{1.25}\text{Nb}_{0.25}\text{Mn}_{0.5}\text{O}_2$ material. *Solid State Ion.* **2019**, *339*, 114999.